Proceedings of
11th European Conference on Turbomachinery Fluid dynamics & Thermodynamics
ETC11, March 23-27, 2015, Madrid, Spain

THE INFLUENCE OF LABYRINTH FLOWS ON THE AERODYNAMIC PERFORMANCE OF AN AXIAL COMPRESSOR

D. Flores and J. R. Seume

Institute of Turbomachinery and Fluid Dynamics - Leibniz Universität Hannover
Appelstrasse 9, Hannover, Germany, e-mail: flores@tfd.uni-hannover.de

ABSTRACT

The interaction between the main and the secondary flow caused by leakage through labyrinth seals lowers the overall performance of an axial compressor. In this study, three cavity outlet variants have been implemented in the third stage of a four-stage high-speed axial compressor in order to investigate the influence of the injection of leakage mass flow into the main flow path. Three-dimensional steady RANS simulations using the SST turbulence model and the multi-mode transition model are performed for all configurations. For the main flow path of the shroudless configuration, the turbulence model predicts the total pressure profiles at the design operating point with sufficient accuracy. Due to the cavity discharge angle of the most efficient configuration, the leakage mass flow slows the main flow near the hub. When this main flow is restrained, the axial component of the main flow near the hub is reduced. This reduction increases the flow angle, leading to a better flow distribution near the hub zone at stator inlet. In addition, the reduction of the axial velocity allows better thermal mixing between the main flow and the leakage flow, increasing the main flow temperature near the hub.

NOMENCLATURE

$C_{1..3}$	Cavity configuration	CDA	Controlled Diffusion Airfoil
H_1	Clearance height in m	CFD	Computational Fluid Dynamics
$\dot{m}$	Mass flow in $\frac{kg}{s}$	CHP	Choke point
M	Mach number	DLR	German Aerospace Center
Re	Reynolds number	DOP	Design operating point
V_{ax}	Axial velocity in $\frac{m}{s}$	IGV	Inlet guide vane
V_r	Radial velocity in $\frac{m}{s}$	ILP	Increased loading point
V_t	Tangential velocity in $\frac{m}{s}$	LE, TE	Leading edge, Trailing edge
V_m	Meridional velocity, $\sqrt{V_{ax}^2 + V_r^2}$ in $\frac{m}{s}$	RPM	Revolutions per minute
y^+	Non-dimensional wall distance	R, S	Rotor, Stator
α	Flow angle, $tan^{-1}(\frac{V_t}{V_m})$ in $^\circ$	SST	Shear stress transport
η_{is}	Isentropic efficiency	$TRACE$	Turbomachinery Research Aerodynamics Computational Environment
Π_{total}	Total pressure ratio		

INTRODUCTION

Impending long-term environmental regulations for civil gas turbines and power plants aim to gradually reduce fuel consumption and emissions. This means that losses in compressors and turbines have to be reduced in order to operate within the regulations. Therefore, more accurate predictions are needed in the axial compressor design chain. Effective numerical methods need to be robust in order to predict the most complex fluid phenomena throughout the operating range of an axial compressor. The numerical compressor modeling is commonly based on methodical assumptions

like mixing-plane or pitch-scale, and geometrical considerations such as fillet radii, cavities and cold rotor tip-clearance due to limitations in computational resources. Based on these assumptions, the present investigation attempts to improve the understanding of the interaction between the main flow and secondary flows caused by labyrinth seals. In the last 20 years, the effects of stator shroud leakage flows on the main flow path have been investigated both experimentally and numerically. The findings convincingly show that leakage flow plays a significant role in compressor efficiency prediction. 3D CFD models give accurate flow details and sufficient agreement with test data when modeling stator cavities. However, the engineering design chain of the turbomachinery industry requires faster and more efficient models. Wellborn and Okiishi (1996) found experimentally a linear correlation between the seal-tooth clearance and the drop in compressor pressure rise. Heidegger et al. (1996) numerically observed that the tangential velocity of the leakage flow increased through the seal cavity. As a consequence, the flow incidence on the stator blade adjacent to the hub increased. Naylor et al. (2009) developed steady three-dimensional multi-stage computations with a one-dimensional model to evaluate the compromise between predictive accuracy and computational effort. Their numerical calculations achieved good agreement at peak efficiency. However, they failed to properly predict the complete speed-line. They also showed that a model with no shroud leakage predicts higher efficiency at the design point by approximately 1% in comparison to other models. Becker et al. (2009) investigated the impact of real cavity geometries numerically in a 4.5 stage high-speed axial compressor, comparing the non-linear harmonic approach with conventional methods. Additionally, they evaluated the effect of a transitional model. They found that the introduction of shroud cavities leads to an overall efficiency decrease of 0.25% and a flow function deficit of 0.05% compared to the cavity-free model. The transition model increased the flow function by 0.23% and efficiency by 0.65% in comparison to the fully turbulent model.

With time-resolving simulations some fluid phenomena can be characterized and observed even more fully, e.g. Fröbel et al. (2010) carried out three-dimensional steady and unsteady simulations including shroud cavities in a 1.5-stage transonic axial compressor. They presented a sensitivity study of two different seal fin heights (SFH). For an increased cavity mass flow rate, the peak efficiency is reduced by approx. 1 pts when compared to the steady nominal SFH. In addition, the unsteady case showed an efficiency increase in the rotor row of approximately 0.25 % points. Kato et al. (2011) investigated the effects of seal-cavity flows on an axial compressor by means of three-dimensional unsteady RANS simulations. The actual cavity geometries of the test rig were approximated by a group of rectangles. Two cases were compared, one shroud-less and the other with cavities. The latter case showed a 1.7% point degradation in efficiency from the first case. They identified windage heating and a loss increase in the middle stages as the main contributors to performance degradation. The temperature rise due to windage causes an approx. 0.5% point drop in overall efficiency. Yamagami et al. (2011) performed unsteady three-dimensional calculations in a multi-stage high-speed axial compressor, focussing on the impact of real geometry modeling with different numerical approaches on the prediction accuracy. They found that predicted mass flow rates are about 2.5% higher than the test data, while the numerically predicted overall efficiency is reduced by 1.7% points by seal cavities. The present study attempts to show which of these effects can be identified even in steady CFD simulations.

TEST RIG

The experimental data for the validation of the shroudless simulations are taken from a high-speed axial compressor rig. It comprises of four stages with inlet guide vanes (IGV) (Figure 1). Detail A shows the configuration C_3 with the angle of 135° with respect to main flow path, depicted in Figure 2c. The compressor blading is entirely composed of controlled diffusion airfoils (CDA). At a maximum rotational speed of 18000 RPM, an overall total pressure ratio of 2.98 at a maximum

isentropic efficiency of 88.6% is reached. Details of the compressor design are listed in Table 1. The flow field between the blade rows was traversed radially and circumferentially over one pitch and measured with a pneumatic four-hole probe. The inlet flow conditions were determined with a Prandtl tube and a temperature probe, and two rakes in the outlet diffuser determined the outlet flow conditions. Efficiency and overall total pressure ratio were calculated from averaged inlet and outlet quantities. The measurements were performed using the reference cavity shown in Figure 2(d). None of these measurements included any of the cavity proposals shown in Figure 2a to 2c. Further details of the rig and the measurement techniques are given in Braun and Seume (2006) and Braun (2007).

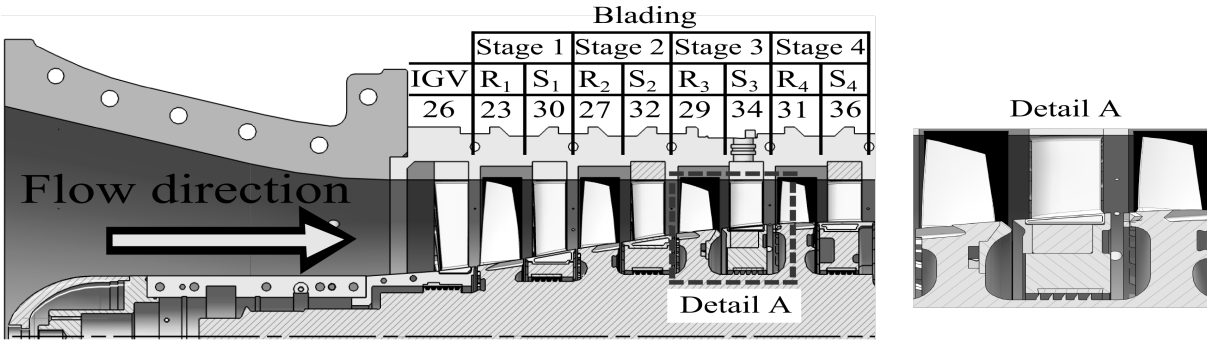

Figure 1: Longitudinal view of the axial compressor and blade count

Table 1: Axial compressor features at design operating point

Parameter	Symbol	Value	Units
Rotational speed	-	17100	RPM
Inlet mass flow	$\dot{m}$	7.82	kg/s
Inlet total pressure	P_i	60000	Pa
Interstages axial velocity	V_{ax}	150...190	m/s
Inlet Mach number	M	0.5	-
Isentropic efficiency	η_{is}	89.8	$\%$
Reynolds number at stator 3	Re	$5.6x10^5$	-
Chord stator 3	c	0.035	m

NUMERICAL MODEL

Cavity Configurations

In practical applications, an axial compressor does not only operate at the design point. Thus, the investigation includes different operating points along the speed line of 17100 RPM. The cavity leaking jet strongly influences the inlet and outlet velocity profiles of the main flow near the stator hub as found by Flores and Seume (2014). As a consequence, the leakage flows spoil the performance of the last stages of the compressor with low aspect-ratio blading. The third stage of the compressor was therefore chosen as the point of modification. Three different configurations of cavity outlets are proposed: C_1=45° (cavity slot pointing in the main flow direction), C_2=90° (cavity outlet slot perpendicular to the main flow path) and C_3=135° (cavity outlet slot pointing against the main flow). Figure 2 shows the three different configurations, along with the original configuration. The original configuration is not investigated in this paper. The axial gap widths in Figure 2 are expressed as a percentage in terms of the third stator chord. Although the leakage mass flow has a strong impact

on the losses when seal clearance is varied as was shown by Flores and Seume (2014), this paper only considers a constant seal clearance of 1.7% (H_1) with respect of the third stator chord to better distinguish and analyze the influence of the cavity outlet angle.

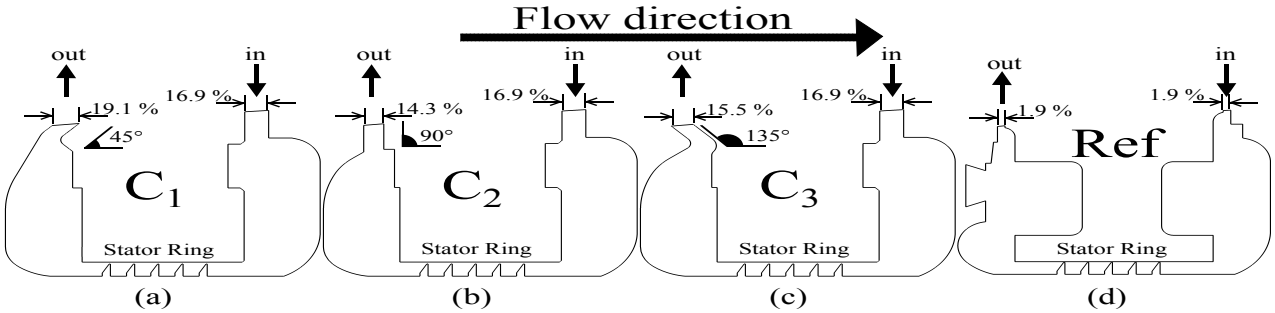

Figure 2: Cavity configurations (all dimensions relative to third stator chord)

Flow Solver

The simulations are performed with the Turbomachinery Research Aerodynamics Computational Environment (TRACE) solver developed by the German Aerospace Center (DLR) at the Institute of Propulsion Technology. TRACE is a multi-purpose, three-dimensional, steady and unsteady, parallelized multi-stage Reynolds-Averaged Navier-Stokes flow solver for structured and unstructured meshes, specifically developed to simulate turbomachinery flows. For flux computations, the spatial discretization uses a total variation diminishing-upwind-scheme (TVD) by Roe with a second-order MUSCL-extrapolation. Numerical oscillations are avoided with the use of a Van Albada flux limiter. Temporal discretization for steady-simulations uses a first-order implicit Euler backward scheme. Detailed information can be found in: Engel (1997), Kügeler (2004), Nürnberger (2004).

Discretization

The mesh of the main flow is created with the multi-block structured grid generator G3DHexa developed by DLR. Every blade passage was meshed with an O-C-H topology, as shown at the midspan of the third stage in Figure 3a. The grid is carefully refined radially in the hub area as shown in Figure 3b. 147 points are used to define the grid radially, and 25 points are placed in the tip-clearance gap of every rotor row. The radial gap of each rotor row is considered as a cold tip for all configurations because warm clearance measurements are not available. The boundaries of the cavity computational domains are defined by the rotor shaft and the stator inner ring. The cavity seal-fin clearance with a height of 1.7% (H_1) relative to the third stator chord is discretized with 24 grid points in the radial direction. Each blade row and each cavity has approximately one million cells. The entire compressor mesh has approximately nine million cells.

The compressor domain consists of only one pitch of every blade row in order to reduce the computational effort, although the assumption of simulating a single pitch and considering the flow as axi-symmetric is not optimal. Heidegger et al.(1996) found only small differences between multi-blade solutions and axi-symmetric flow solutions when using mixing-planes in the rotor-stator interfaces. Fillet radii are included in every blade row. The inclusion of fillets in upstream stages hinders the coupling of the remaining cavities because of the reduced axial gap between rows, therefore they were not simulated.

In order to resolve boundary-layer flow along blades, hub and tip surfaces accurately, a low-Reynolds is used with a non-dimensional wall distance y^+ of approximately 1 and a maximum expansion ratio of 1.2. All computations are carried out with the two-equation $k-\omega$ SST model by

Menter (2003). Additionally, the multimode-transition model by Kozulovic (2004) and a stagnation-point anomaly correction was used.

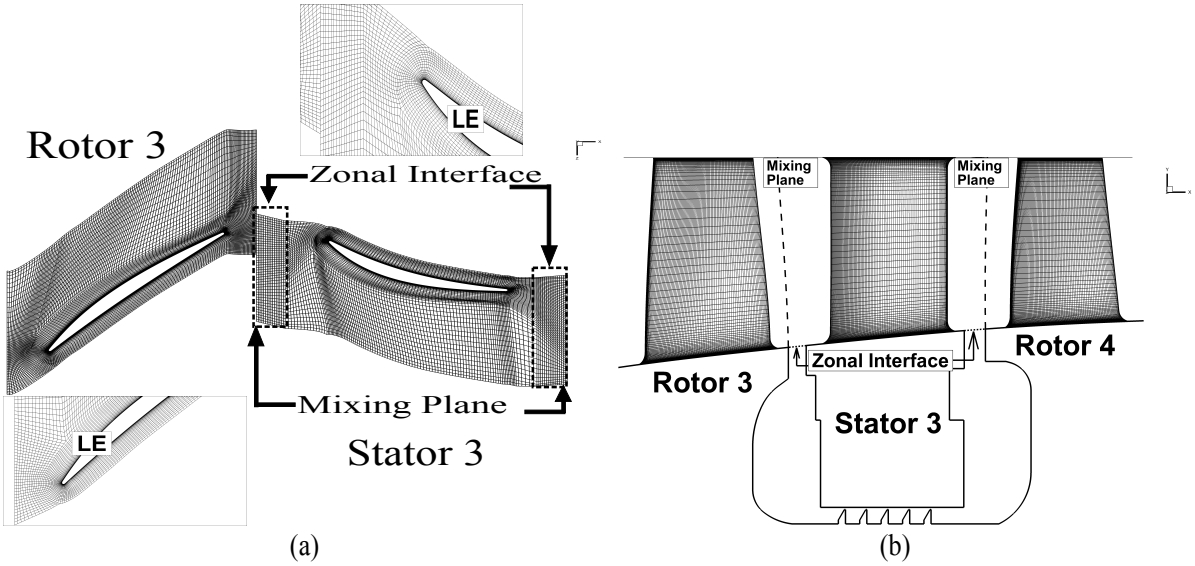

Figure 3: Mesh details of third stage
(a) Blade-to-blade view (b) Meridional view

Boundary conditions and Fluid model

The fluid is air, modeled as an ideal gas and viscosity is computed using Sutherland's law. All domain surfaces are considered as no-slip adiabatic walls. The boundary conditions for the simulations are taken directly from rig measurements at the design operating point. At the inlet, circumferentially averaged radial profiles of total pressure and temperature are specified. The outflow boundary condition was either mass flow or static pressure driven, depending on the operating point. A mass flow condition is imposed at the operating points where there is increased loading. A mixing-plane approach is used in all rotor-stator interfaces (Figure 3b). For cavity coupling a zonal interface approach is used, which is a conservative mixed-cell approach of second-order accuracy (Yang et al. 2003).

RESULTS

Convergence criteria

The complexity of cavity simulations arises from the interaction between high Mach number flows in the main channel and pressure driven low Mach flow regimes in the cavities. The fidelity of simulation results depends strongly on the convergence level. Thus, the quality of the numerical models is evaluated by means of the global parameter's convergence in the main flow path, namely mass flow $\dot{m}$, total pressure ratio Π_{total} and isentropic efficiency η_{is}. The convergence of these parameters is compared for three operating points: maximum mass flow (A/CHP), design operating point (B/DOP), and increased loading (C/ILP). All simulations use identical boundary conditions aside from the outlet conditions. Operating points A and B used static pressure, and C used mass flow at the outlet to stabilize the numerical scheme as no convergence could be achieved with a pressure outlet condition. In Figures 4a to 4c the convergence monitors of the configuration's third stage at 90° with the tightest clearance H_1 are shown (see Figure 2b). Figures 4d to 4f depict the monitors of mass flow, total pressure and total temperature at cavity outlet. The variables are normalized with respect to inlet conditions.

For the operating point A, all quantities converge within approximately 10,000 iterations except for isentropic efficiency, for which the simulations require additional 60,000 iterations to reach relative constancy (Figure 4c). At the design operating point B, the mass flow residual converges after 20,000 iterations, the total pressure ratio Π_{total} residual converges the quickest with 10,000 iterations, and the isentropic efficiency η_{is} needed 70,000 iterations to reach constancy. For the increased loading point C, initialized with a converged flow solution, the turbulence model reaches a fair residual level of stability at 20,000 iterations. However, it was given 10,000 more iterations to assure complete constancy. All residuals oscillated strongly during the first 10,000 iterations. A similar convergence trend is found for all cavity models. They required between 50 to 60% increased run time when compared to the shroudless model. Despite the simulations' use of steady state conditions, the inclusion of cavities leads to oscillations of the monitors in all points except for point C (Figures 4d to 4f). This periodicity is attributed to the cavities' inclusion because the shroudless model did not show this behaviour in the third stage monitors.

Comparing the mass flow residuals in Figures 4a and 4d, shows that the leakage mass flow at the cavity outlet increases inversely to that at the third stator inlet along the speed line from operating point A to C. The total pressure monitors at the cavity outlet depicted in Figure 4e show an increase from a low to high rate from point A to C as expected. The monitors illustrated in Figure 4f show that the total temperature rate converges slowly for operating points A and B up to 70,000 iterations, presumably because of the slow convergence of the temperature gradient in the cavity.

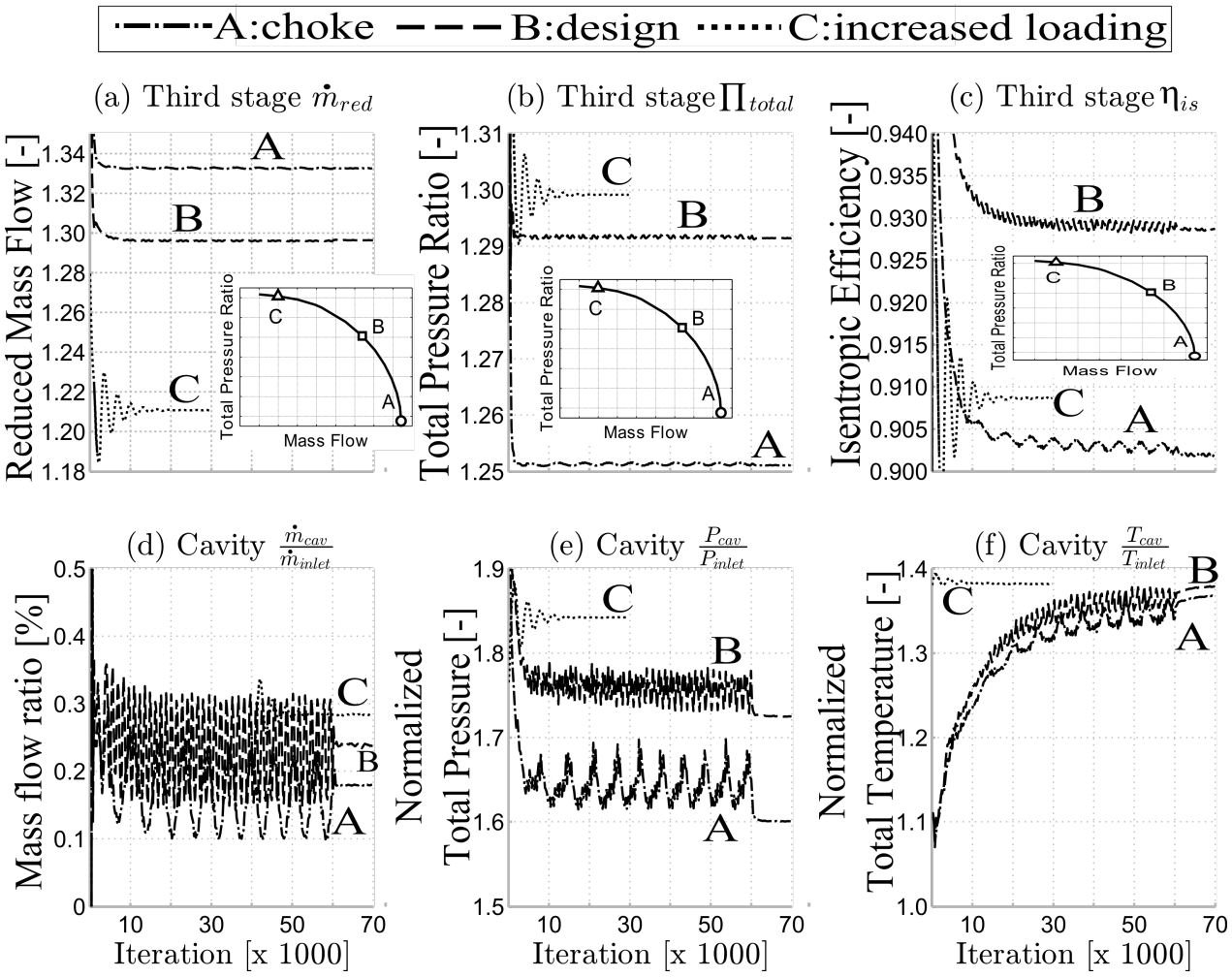

Figure 4: a-c: Convergence residuals of the third stage, d-f: cavity outlet monitors

Baseline correlation

The validation of the model without cavities (WoC) is crucial to assure confidence in the simulation results of the following operating points. Therefore, experimental data (Braun 2006) and computed radial profiles of the shroudless model were compared to validate the well-converged flow field of the design point B (Figure 4), and simultaneuosly to visualize major deviations. Similar to the validation by Flores and Seume (2014), Figure 5 compares the circumferentially-averaged total pressures and total temperatures for stators and rotors. The radial profiles for both variables were normalized with respect to appropriate inlet conditions. The error quantifications for the experimental data appear to be almost negligible with respect to the corresponding variables ($P_{tot} \pm 0.0132\%$ and $T_{tot} \pm 0.002\%$).

For the design operating point B, the distributions of total pressure in the stators agree well with experimental profiles from 30% to 90% span (Figure 5a). A similar tendency is observed in the total pressure variation in the experimental and numerical data for the rotor rows (Figure 5b). Near the hub the differences are greater than mid-span due to the cavities' effect on the test rig. The total temperature profiles show good agreement only for the IGV. In the remaining stators an increased temperature rise is observed in the blade tip region. The total temperature profiles in the tip area of the rotor rows show similar discrepancies (Figure 5b). At mid-span, experimental and numerical profiles of total pressure and total temperature show good agreement. The largest deviation in total temperature profiles is observed in the last stage.

The computed total temperature profiles predict a lower temperature rise at the tip. The lack of precision in the tip area can be attributed to two main reasons: Firstly, the rotor rows are simulated with cold-tip rotor clearances instead of the smaller clearances of the experimental setup. Secondly, steady state simulations do not resolve unsteady flow effects like tip vortices.

Overall Performance

The influence of the cavities on the axial compressor performance is evaluated through the integral flux-averaged isentropic efficiency and the total pressure ratio. Figures 6a to 6c show the comparison of the overall performance of the shroudless model and the three configurations with clearance H_1. Experimental data serves as a reference. The overall performance is presented because the influence of the leakage mass flow not only affects the stator performance where the cavity is being analyzed, but also changes the stator exit flow conditions, which in turn modify the performance of the downstream stages. The shroudless model (WoC) is simulated with boundary conditions taken from the experimental design operating point (ⓘ) and validated through the radial profile comparison already shown in Figure 5.

The computed mass flow of the shroudless model agrees very well with the measurements at the design operating point. However, the computed efficiency is approximately 2 pts higher. This efficiency overprediction can be traced to the lack of accuracy in the temperature profiles (Figure 5). Further simulations reveal that the entire computed speed-line is displaced towards the left with respect to the experimental line, including the numerical point of best efficiency (ⓘⓘ). The WoC model reaches a peak efficiency of 92.2% at a lower mass flow than the experimental mass flow.

Figures 6b shows that the WoC model predicts the total pressure ratio and mass flow rate at the design point (ⓘ) with sufficient agreement. Towards the increased loading point, the inclusion of the cavity tends to bend the curve of total pressure ratio. At design operating point (ⓘ), the reduced mass flow and the total pressure ratio practically remain unaltered when the cavity outlet angle increases from C_1 to C_3.

Figure 6c illustrates the deviation of isentropic efficiency with respect to mass flow rate for the WoC model and the cavity variants. The efficiency deviation with the tightest clearance H_1 shows a

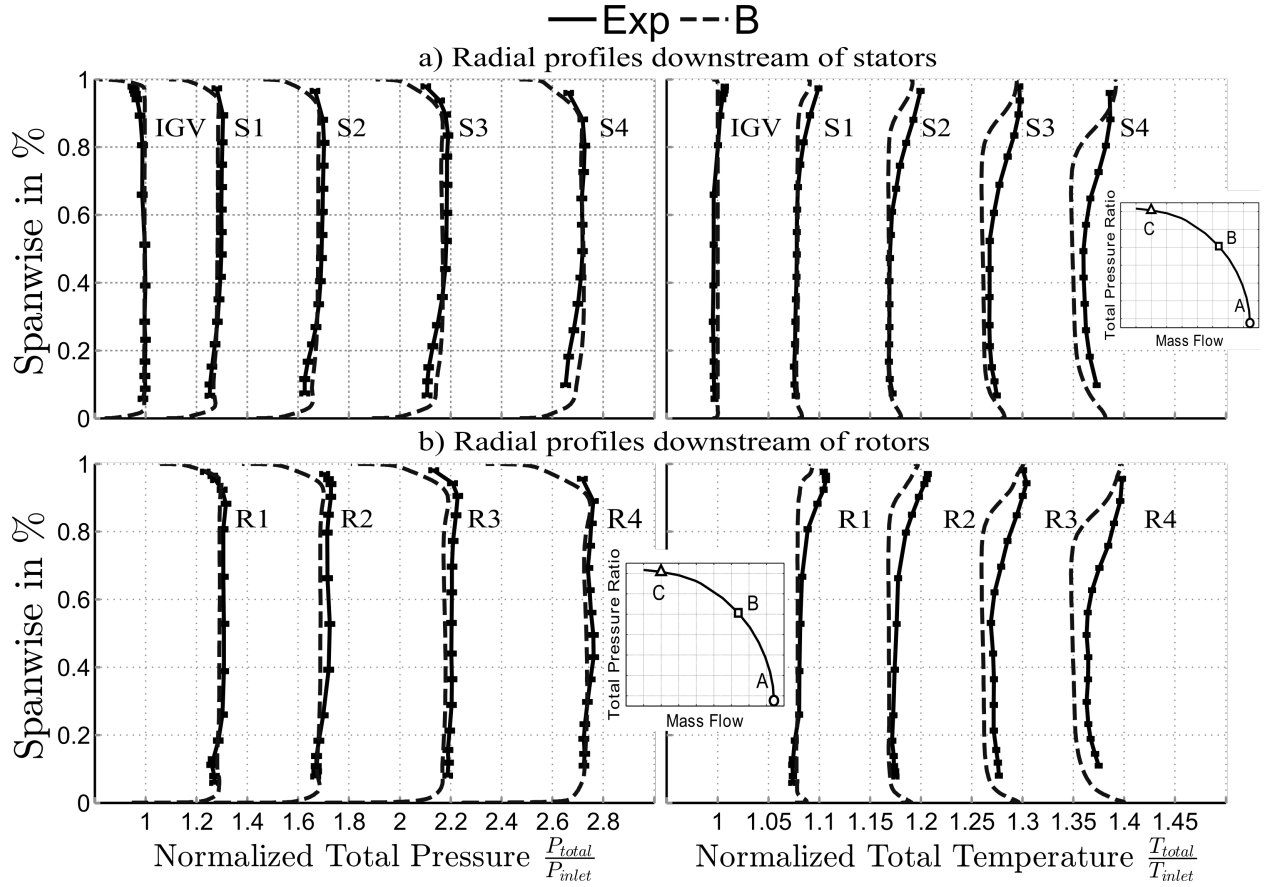

Figure 5: Comparison of computed radial profiles (shroudless model) with experimental data at the design operating point

moderately deteriorating slope. The difference between the three cavity angles is evident along the entire speed-line. Configuration C_3 shows the lowest deterioration along the entire computed isentropic efficiency line, even in the increased loading zone. Herein the difference it is much noticeable, C_1 deteriorates 0.329 %, C_2 0.248% and C_3 0.172 % (see Table 3).

Figure 6d depicts the isentropic efficiency of the third stage. The measurement planes are defined at third rotor inlet and third stator exit, in order to include the effects of the cavity in the isentropic efficiency calculation. The deviations are greater than those for overall efficiency shown in Figure 6a. The inclusion of the cavity geometry in the model is detrimental to the stage performance; however the modeling trends are more realistic with respect to experimental data.

Table 2 shows the performance comparison at the design point (DOP) for the cavities with clearance H_1, except for the last column which shows the efficiency deviation for the increased loading point (ILP). The three configurations and the shroudless model predict both mass flow rate and total pressure ratio very well at design operating point. Despite good agreement of the WoC model, it overpredicts isentropic efficiency by 2 pts in comparison with the experimental method. The 135° variant shows the smallest drop in isentropic efficiency with respect to the WoC model at design point and increased loading point.

Cavity effects on stator inlet and outlet over the design line

Three configurations inject the secondary flow into the main flow path such that it increases the momentum in the main low, which translates into an increase or decrease in velocity near the hub depending on the cavity angle. Figure 7 shows the effect of the cavity angle on the velocity profiles

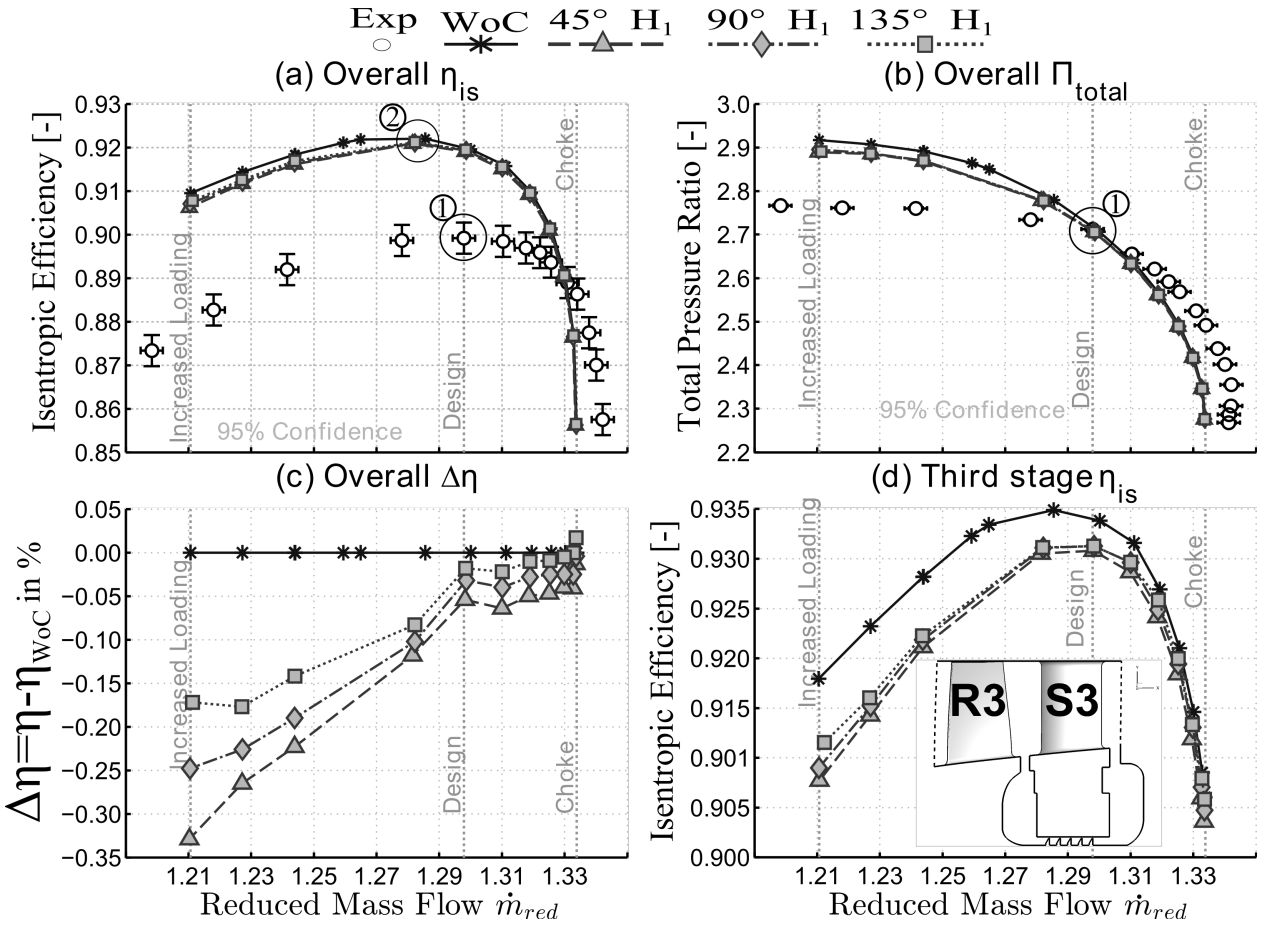

Figure 6: Axial Compressor Overall Performance

measured at 10.33 % of chord upstream of the third stator leading edge (Figure 7j). The profiles are confined to less than 30 % of span, the profiles are negligibly affected near the tip. The profiles are normalized with respect to the corresponding maximum velocity. Major differences are observed below 3% of span (Figures 7f to 7j). In this zone, the WoC model generates higher velocities except for the radial velocity V_r. The inclusion of cavities reduces the axial velocity near the hub. The reduction in axial velocity diminishes gradually from 68% to 49% to 38% and 37% as the cavity angle increases. This reduction near the hub causes an increase in the axial velocity profiles from 5% to 30% of span. The leakage mass flow restrains the main flow below 3% of span, while pushing the main flow towards the casing thus accelerating the main flow between 5% and 7% of span. In this zone, the flow acceleration displaces the axial velocity profile by approx. 2% in the direction of the main flow. The cavities change the tangential velocity profiles slightly (less than 1%) from 5% to 30% of span. As expected, the WoC model shows the highest tangential velocity with maximum values of 99.8%, 98.7%, and 95.9% as the cavity angle is increased. The highest tangential velocities are located at 0.94%, 1.77%, 2.05%, and 2.33% of span following the cavity angle increase. The trends change from 0.12% to 0.7% of span, whereas the cavity configuration with an angle of 135° produces the highest tangential velocity. The comparison of radial velocities reveals that below 0.5% of span, the cavity with an angle of 45° increases the rate by 50% compared to the two remaining configurations. It retains its position as the fastest radial velocity profile along the entire spanwise. The cavity with an angle of 135° starts to deviate from the 90° cavity from 0.5% to 20% of span on, indicating a lower rate than the remaining cavity configurations. The meridional velocity profiles follow similar trends to those shown in Figures 7a and 7f, which indicates that the axial velocity has

Table 2: Overall predicted performance at the design mass flow as shown in Figure 6 (cavities with clearance H_1 = 1.7%)

Configuration	$\dot{m}_{red}$ at DOP	Π_{Total} at DOP	η_{is} in % at DOP	$\Delta\eta$ in % at DOP	$\Delta\eta$ in % at ILP
Experiment	1.298	2.713	89.92	-	-
WoC	1.3	2.706	91.96	0	0
$C_1 = 45°$	1.298	2.706	91.906	-0.054	-0.329
$C_2 = 90°$	1.299	2.706	91.928	-0.032	-0.248
$C_3 = 135°$	1.298	2.706	91.942	-0.018	-0.172

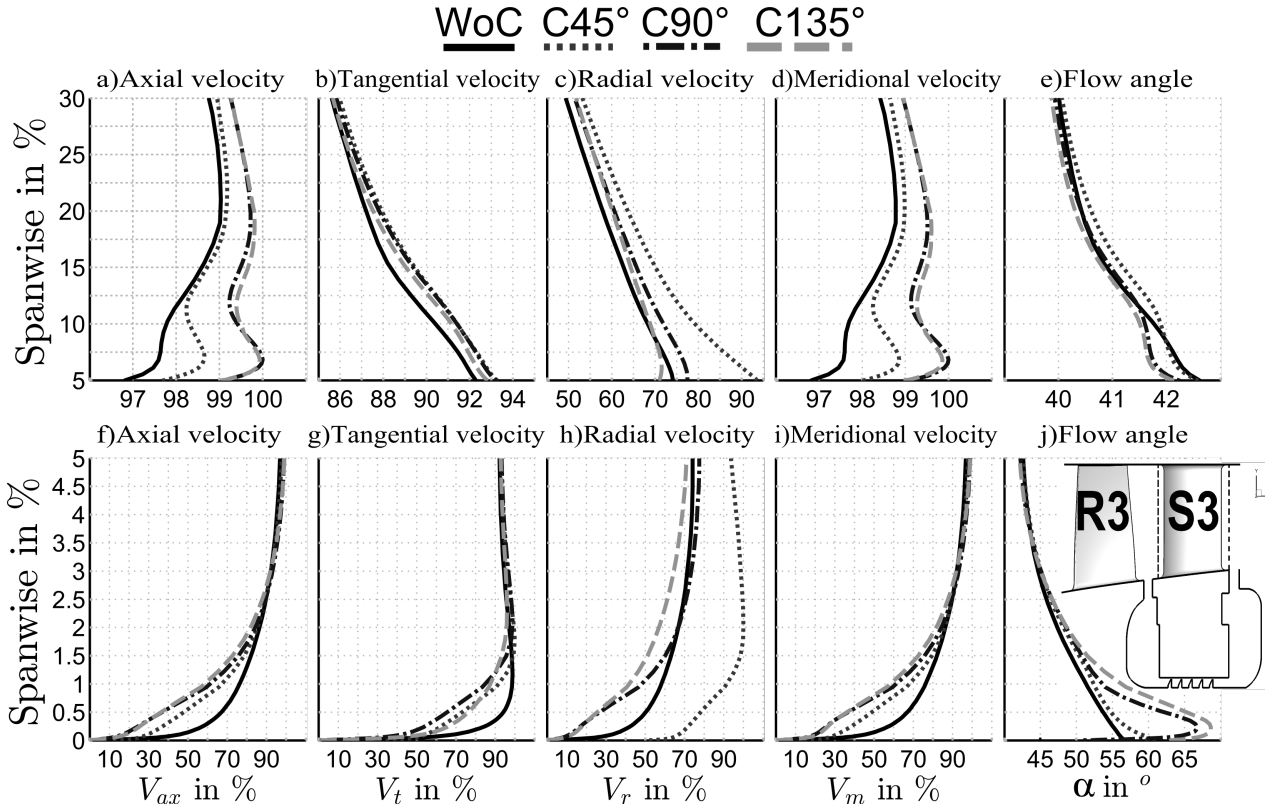

Figure 7: Velocity and flow angle profiles over the design line with clearance $H_1 = 1.7\%$ at stator inlet (point 1 in Figure 6c)

the strongest influence on the meridional velocity. The deviation of flow angle between 5% and 30% of span is below 1°. The profiles start to deviate from each other below 3% of span and the highest deviations are observed below 0.5% of span. In this zone, the velocity profile causes the flow angle to increase.

Table 3 shows the velocities for the highest flow angle. The WoC model has the lowest flow angle and the highest velocities, except for the radial velocity V_r because there is no radial outflow from the cavity in this case. As cavity angle increases from C_1 to C_3, the flow angle increases because the axial velocity decreases. Nevertheless, the flow angle and axial velocity difference between C_2 and C_3 is scarcely 2° and 1.28%, respectively. The tangential velocity difference is 11.82%, which indicates a difference of 2° in tangential velocity. In fact, the leakage mass flow of the cavity with 45° offers less resistance against being injected into the main flow. Due to the cavity angle, the axial and radial

Table 3: Velocity variations at highest flow angle with clearance $H_1 = 1.7\%$

Configuration	α in $^\circ$	Spanwise in %	V_{ax} in %	V_t in %	V_r in %	V_m in %
WoC	56.25	0.19	54.04	82.91	39.72	54.01
$C_1 = 45^\circ$	57.59	0.19	34.42	59.63	70.3	35.75
$C_2 = 90^\circ$	66.66	0.19	23.08	50.63	15.08	23.77
$C_3 = 135^\circ$	68.67	0.19	21.8	62.45	16.12	24.74

velocities increase and the flow angle diminishes despite the fact that the tangential velocity rate stays high.

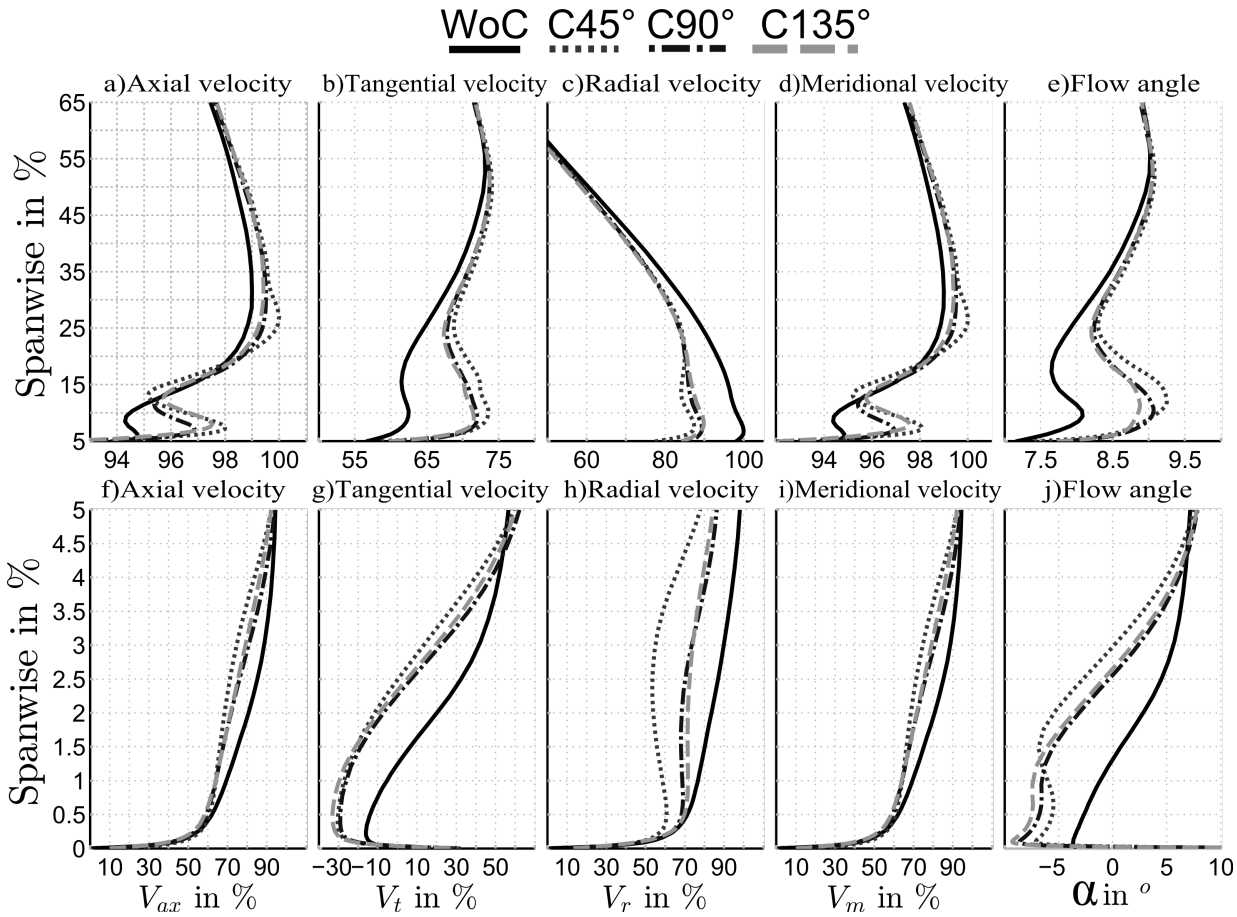

Figure 8: Velocity and flow angle profiles over the design line with clearance $H_1 = 1.7\%$ at stator outlet (point 1 in Figure 6c)

Naturally the stator exit profiles will also change as the cavity flow modifies the stator inlet profiles. In Figure 8, a comparison of velocity profiles at an axial position of 13.31 % of third stator chord downstream of third stator trailing edge shows that all velocities increase except the radial velocity between 5 to 10% of span. Axial and tangential velocities increase by 2-3 % and 10 %, respectively with respect to the WoC model while radial velocity decreases by 10 %. The flow angle increases by approximately 1°, but the C_3 model shows the lowest deviation compared to the two remaining cavity configurations. All radial profiles below 5 % of span depict lower values with respect to the WoC model as shown in Figures 8f to 8j. At 3 % of spanwise, there is a difference of 15 %, 30 %, 36 % and 5° in the axial, tangential, radial velocity and flow angles, respectively between the WoC and

C_1 model. The meridional velocity behaves similarly to the axial velocity, by definition. Below 3 % of span the flow angle shows negative values mostly driven by the tangential velocities. By looking at all of the radial profiles, it can clearly be seen that the cavity leakage flow modifies the stator exit profiles which in turn modify the performance of the next downstream stage.

CONCLUSIONS

The influence of three cavity variants implemented in the third stage of a four-stage high-speed axial compressor has been investigated in order to better understand the interaction between the main flow and the leakage flow caused by labyrinth seals. Cavity geometries have a strong influence on the compressor performance per se. The following conclusions can be drawn from the modeling experience in this work:

(1) The reliability of a model cannot be sufficiently determined by monitoring only mass flow and total pressure ratio. It is highly recommended that the isentropic efficiency is monitored during the correlation-validation process in order to ensure reliable results.

(2) A comparison of total pressure for the CFD analysis of the shroudless model with the experiment shows that the SST turbulence model predicts the same total pressure profiles at the design operating point with sufficient accuracy.

(3)The lack of agreement between the CFD model and experimental data at the tip with respect to total temperature profiles suggests that a study of the rotor tip clearance and unsteady simulations are necessary to increase accuracy.

(4)At the design operating point, the shroudless model predicts (as stated above) the total pressure ratio and mass flow rate with sufficient accuracy. Nevertheless, it overpredicts isentropic efficiency by approx. 2 pts. The good agreement of total pressure ratio with the experimental data confirms an accurate prediction of total pressure profiles.

(5)The main physical insights gained here are: that the cavity outlet angle $C_3 = 135^\circ$ achieves the lowest isentropic efficiency reduction when compared to the case without cavities for the clearance equal to 1.7% over the entire speed-line. The reason for this is that, due to the cavity angle of the configuration C_3 the leakage mass flow slows down the main flow near the hub. When this main flow is restrained, the axial velocity of the main flow near the hub is reduced. This reduction turn increases the flow angle, leading to a better flow distribution near the hub at the stator inlet. In addition, the reduction of the axial velocity allows better thermal mixing between the main flow and the leakage flow, which increases the main flow temperature near the hub.

ACKNOWLEDGEMENTS

D. Flores gratefully acknowledges the support of the Mexican National Council of Science and Technology (CONACyT) and the German Academic Exchange Service (DAAD). Both authors would like to acknowledge DLR for providing TRACE and RRZN (Regionales Rechen-Zentrum fuer Niedersachsen) for using their cluster.

REFERENCES

Becker, B., Kupijai, P, and Swoboda, M., 2009. "High Fidelity CFD on a High-Speed 4.5-Stage Compressor by means of the Non-Linear Harmonics Approach and Transition Model". Proceedings of the 8th European Conference on Turbomachinery Fluid Dynamics and Thermodynamics.

Braun M., 2007. "Experimentelle und numerische Untersuchungen einer vorwaertsgepfeilten Beschaufelung in einem mehrstufigen hochbelasteten Axialverdichter". Dissertation, Gottfried Wilhelm Leibniz Universitaet Hannover.

Braun M. and Seume J., 2006. "Forward Sweep in a Four-Stage High-Speed Axial Compressor". ASME Conference Proceedings, GT2006-90218.

Engel K., 1997. ”Numerische Simulation der Instationaeren Stroemung in Turbomaschinenkomponenten”. Dissertation, Universitaet-GH Essen.

Flores, D. and Seume, J., 2014. ”Selecting cavity geometries for improving the aerodynamic performance of an axial compressor”. ASME Conference Proceedings, GT2014-25328.

Fröbel, T. and Kau H., 2010, ”Numerical Investigation of Unsteady Flow Phenomena in an HP Axial Compressor Incorporating Stator Shroud Cavities”. 46th. AIAA/ASME/SAE/ASEE Joint Propulsion Conference, AIAA 2010-6532

Heidegger, N., Hall, E., and Delaney, R, 1996. ”Stator Seal Cavity Flow Investigation”. NASA Contractor Report 198504, Allison Engine Company, Indianapolis, Indiana, USA.

Kato, D., Yamagani, M., Tsuchiya, N., and Kodama, H., 2011. ”The Influence of Shrouded Stator Cavity Flows on the Aerodynamic Performance of a High-Speed Multistage Axial-Flow Compressor”. ASME Conference Proceedings, GT2011-46300.

Kuegeler E., 2004. ”Numerisches Verfahren zur genauen Analyse der Kuehleffektivaet filmgekuehlter Turbinenschaufeln”. Dissertation, Ruhr-Universitaet Bochum.

Menter, F., 2009. ”Review of the Shear-Stress Transport turbulence model experience from an industrial perspective”. International Journal of Computational Fluid Dynamics, 23, pp. 305-316.

Naylor, E., Montomoli, F., Hodson, H., and Lapwoth, L., 2009. ”Numerical Modeling of Cavities in Multistage Axial Compressors”. ISABE-2009-1186.

Nuernberger D., 2004. ”Implizite Zeitintegration fuer die Simulation von Turbomaschinenstroemungen”. Dissertation, Ruhr-Universitaet Bochum.

Wellborn, S. and Okiishi, T., 1996. ”Effect of Shroud Stator Cavity Flows on Multistage Axial Compressor Aerodynamic Performance”. NASA Contractor Report 198536, Iowa State University, Ames, Iowa, USA.

Yamagani, M, Kodama, H., Kato., D, Tsuchiya, N., Horiguchi, Y., and Kazawa, J., 2011. ”CFD Modeling Effects on Unsteady Multistage Simulation for a Transonic Multistage Axial Compressor”. ASME Conference Proceedings, GT2011-46198.

Yang, H., Nuernberger, D., Nicke, E., and Weber, A., 2003. ”Numerical investigation of casing treatment mechanisms with a conservative mixed-cell approach”. ASME Conference Proceedings, GT2003-38483.